

INFLATING AND DEFLATING HOT JUPITERS: COUPLED TIDAL AND THERMAL EVOLUTION OF KNOWN TRANSITING PLANETS

N. MILLER¹, J. J. FORTNEY¹, AND B. JACKSON²

¹ Department of Astronomy and Astrophysics, University of California, Santa Cruz, CA 95064, USA; neil@astro.ucsc.edu, jfortney@ucolick.org

² Lunar and Planetary Laboratory, University of Arizona, Tucson, AZ 85721, USA; bjackson@lpl.arizona.edu

Received 2009 May 4; accepted 2009 July 6; published 2009 August 21

ABSTRACT

We examine the radius evolution of close in giant planets with a planet evolution model that couples the orbital–tidal and thermal evolution. For 45 transiting systems, we compute a large grid of cooling/contraction paths forward in time, starting from a large phase space of initial semimajor axes and eccentricities. Given observational constraints at the current time for a given planet (semimajor axis, eccentricity, and system age), we find possible evolutionary paths that match these constraints, and compare the calculated radii to observations. We find that tidal evolution has two effects. First, planets start their evolution at larger semimajor axis, allowing them to contract more efficiently at earlier times. Second, tidal heating can significantly inflate the radius when the orbit is being circularized, but this effect on the radius is short-lived thereafter. Often circularization of the orbit is preceded by a long period while the semimajor axis slowly decreases. Some systems with previously unexplained large radii that we can reproduce with our coupled model are HAT-P-7, HAT-P-9, WASP-10, and XO-4. This increases the number of planets for which we can match the radius from 24 (of 45) to as many as 35 for our standard case, but for some of these systems we are required to be viewing them at a special time around the era of current radius inflation. This is a concern for the viability of tidal inflation as a general mechanism to explain most inflated radii. Also, large initial eccentricities would have to be common. We also investigate the evolution of models that have a floor on the eccentricity, as may be due to a perturber. In this scenario, we match the extremely large radius of WASP-12b. This work may cast some doubt on our ability to accurately determine the interior heavy element enrichment of normal, noninflated close in planets, because of our dearth of knowledge about these planets’ previous orbital–tidal histories. Finally, we find that the end state of most close in planetary systems is disruption of the planet as it moves ever closer to its parent star.

Key words: planetary systems – planets and satellites: general

Online-only material: color figures

1. INTRODUCTION

The precise mass and radius measurements for transiting exoplanets provide information about the planets’ interior structure and composition, which are often apparently unlike that of Jupiter and Saturn. Indeed, it is the incredible diversity of measured radii of transiting planets that has been most surprising. In the solar system, Jupiter and Saturn differ in mass by a factor of 3, while their radii differ by only 18%. However, amongst exoplanets, planets with the same mass can differ in radius by a factor of 2. A hope amongst planetary astrophysicists was that the measurement of the mass and radius, when compared to models, would cleanly yield information on planetary interior composition. Although there are clear examples where this has been done successfully, including heavy element rich planets such as HD 149026b (Sato et al. 2005; Fortney et al. 2006) and GJ 436b (Gillon et al. 2007), in general modelers have been foiled by planets with very large radii, larger than can be accommodated by “standard” cooling/contraction models.

Considerable work has been done in the past several years to understand the large radii of some planets, as well as the radius distribution of the planets as a whole. Explanations for the “anomalously” large planets have fallen into three categories: those that are a current or recent additional internal energy source, which has stalled the interior cooling and contraction (Bodenheimer et al. 2001; Guillot & Showman 2002; Bodenheimer et al. 2003; Gu et al. 2003; Winn & Holman 2005; Liu et al. 2008; Jackson et al. 2008b; Ibgui & Burrows 2009), those that instead merely delay the contraction by slowing

the transport of interior energy (Burrows et al. 2007; Chabrier & Baraffe 2007), and those that invoke various evaporation mechanisms (Baraffe et al. 2004; Hansen & Barman 2007). These are briefly reviewed in Fortney (2008).

Tidal heating as an explanation for these large-radius planets was suggested by Bodenheimer et al. (2001) for HD 209458b and has been revisited frequently by other authors (e.g., Bodenheimer et al. 2003; Winn & Holman 2005; Liu et al. 2008; Gu et al. 2003, 2004; Jackson et al. 2008a, 2008b; Ibgui & Burrows 2009). We note that the mechanism of heating by obliquity tides (Winn & Holman 2005) has been cast in considerable doubt by several authors (Levrard et al. 2007; Fabrycky et al. 2007; Peale 2008).

At this time, tidal heating by orbit circularization is generally believed to be the most important type. The largest uncertainties in the standard tidal theory are the “tidal Q ” value, a standard parameterization of the rate of tidal effects. In this work, we use the standard notation for the planet tidal Q value as Q'_p and the stellar tidal Q value as Q'_s . Jupiter’s Q'_p value has been constrained to be between 10^5 and 10^6 (Goldreich & Soter 1966). For tidal heating by circularization to take place, the planet must either initially have an eccentric orbit or the system must be driving the eccentricity of the planet at recent times.

The former scenario would have the following qualitative stages. The planet is left with an eccentric orbit through planet–planet interactions (Rasio & Ford 1996; Chatterjee et al. 2008; Ford & Rasio 2008). Tides on the star gradually reduce the semimajor axis. These tidal effects accelerate as the semimajor axis decreases. Tides on the planet become more important and

the planet's orbit circularizes, at the same time depositing orbital energy into the planet's interior. Scattering/tidal evolution models of this sort were recently computed by Nagasawa et al. (2008). At this point, the system might be observed to have a fairly circular orbit and a larger-than-expected radius. Ibgui & Burrows (2009) use a coupled tidal–thermal evolution model, quite similar to the one we present here, to show that this scenario might be possible for the HD 209458 system, and by extension, many hot Jupiter planets. Such a model is necessary to self-consistently explain a planet's radius in this picture. One potential issue with this scenario is that it can require large-radius planets to be observed at a “special time” since after the orbit is circularized, the planet may rapidly contract.

Alternatively, some planets might be found in an equilibrium state where their eccentricity is being forced by a third body while at the same time tides on the planet are damping the eccentricity (Mardling 2007). This is an attractive explanation because the planet might be found in an inflated state for a long period of time. Previously, Bodenheimer et al. (2001) calculated the tidal power required to maintain the radius for HD 209458 b, Ups And b, and Tau Boo b, as a function of the assumed core size, in a stationary orbit. Recently, thermal evolution calculations with constant heating have been performed for TrES-4, XO-3b, and HAT-P-1b by Liu et al. (2008), who placed constraints on \bar{e}^2/Q'_p , - where \bar{e} is the recent time-averaged eccentricity of the orbit. These calculations are useful for estimating the required recent tidal heating. In some cases, where the eccentricity is nonzero and a perturber is necessary to invoke, then this constant heating picture might accurately describe the recent thermal history of the planet. In many cases, the eccentricity is observed to be close to zero, which either implies that (1) the planet's eccentricity is at a nonzero equilibrium, but the planet's Q'_p value is much smaller than inferred from Jupiter or (2) the planet's orbit is circularized and this calculation does not apply.

Clearly it is important to accurately measure the eccentricity of inflated systems to determine if either scenario is plausible. For many transiting systems, the eccentricity has been only weakly constrained with several radial velocity points and it is very difficult to distinguish a small eccentricity from one that is truly zero (Laughlin et al. 2005). For systems with an observed secondary eclipse, stronger upper limits on eccentricity can be found based on the timing of the eclipse (Deming et al. 2005; Charbonneau et al. 2005; Knutson et al. 2009). Note that secondary eclipse timing only constrains $e \cos \Omega$, so it is possible that some of these systems have much larger eccentricity, but it is unlikely.

The above possibilities are also consistent with the popular planet formation and migration theories. These planets form while the protoplanetary disk is still present at much larger orbital distances and migrate early in their life to small orbital distances (e.g., Lin et al. 1996). After this initial phase, tidal evolution between the star and the planet occurs on Gyr timescales. The migration mechanism is important because it determines the initial orbital parameters for tidal evolution. There are multiple postulated migration mechanisms.

1. Planet–disk interaction: gravitational interactions between the planet and protoplanetary disk can exert torque on the planet (Ward 1997a, 1997b). These mechanisms tend to circularize the planet's orbit very early on and decrease the semimajor axis. The disk migration timescales are significantly shorter than the lifetime of the disk, as described in Pappalouizou et al. (2007), and references therein.

2. Planet–planet interaction: gravitational interactions with other nearby planets can transfer orbital energy and angular momentum between the two bodies. This can result in quickly decreasing or increasing the orbital distance of one of the planets as well as producing nonzero initial eccentricity orbits. Using N -body simulations, (Rasio & Ford 1996; Weidenschilling & Marzari 1996; Chatterjee et al. 2008; Ford & Rasio 2008) have shown that this effect can be important and can result in the inner bodies having initial eccentricity as large as 0.8, before tidal damping ensues. Other authors have investigated migration with coupled secular driving and tidal friction, which can operate on similar timescales (Wu & Murray 2003; Faber et al. 2005; Ford & Rasio 2006; Fabrycky & Tremaine 2007). There are also a handful of transiting planets that have nonzero eccentricity today, which can be explained by planet–planet interactions. It is also suggestive that many of these eccentric planets are more massive and have longer circularization timescales. Since the circularization time is longer for massive planets, this observation is consistent with the idea that planets of all masses can have large initial eccentricity, but that the lower mass planets have circularized while the massive planets may still be circularizing.

We expect that both of these mechanisms do happen to some extent. Therefore, we assume that a wide range of initial orbital parameters are possible, and we follow the orbital and structural evolution of planets from a wide range of possible initial eccentricities, as described below. In the absence of a theory to predict likely initial eccentricities for a given planetary system, we seek to understand the physics of the evolution from a variety of initial states.

Most of the detected transiting planets currently have small eccentricities consistent with zero. These can be explained by either migration mechanism. If the planet migrated through planet–disk interactions, then it would have zero eccentricity when tidal evolution began. If the planet migrated through planet–planet interactions, then the orbit may have circularized due to tides on the planet.

2. MODEL: INTRODUCTION

In this work, we would like to test the possibility that tidal heating by orbit circularization can explain the transit radius observations for each particular system. A necessary condition for this model is that a self-consistent evolution history can be found that agrees with all of the observed system parameters. To check this condition, we forward-evolve a coupled tidal–thermal evolution model over a large grid of initial semimajor axis and eccentricity for each system. We perform this test for $Q'_s = 10^5$, $Q'_p = 10^5$ and $Q'_s = 10^5$, $Q'_p = 10^{6.5}$. Also, for each system with nonzero current eccentricity, we emulate an eccentricity driving source by performing runs with an eccentricity floor equal to the observed value. Later we also explore some higher Q'_s cases.

To properly understand the planet's thermal evolution, it is necessary to couple the planet thermal evolution to the orbital–tidal evolution. Generally, planets with initial semimajor axis of 0.1 AU or less will spiral into the star in Gyr timescales (Jackson et al. 2008a). This has a large impact on the incident flux on the planet, and therefore the loss of intrinsic luminosity of the planet. For some systems, this more efficient cooling at early times makes it possible to achieve smaller radii at

the present. As the planet moves closer to the star, the tidal effects accelerate. If the orbit is eccentric, then at some point the planet's orbit undergoes a period of circularization. At this time a significant amount of orbital energy is deposited into the planet, which increases its radius. The question of this work is whether, at this stage, the system's observables (a , e , age, R) can simultaneously be achieved in the model. After this stage, the planet may lose mass by Roche lobe overflow (Gu et al. 2003), which can temporarily prevent the planet from falling into the star. However, the planet's destiny is to fall into the star (Levrard et al. 2009; Jackson et al. 2009). These final stages of the planet's life, including the mass loss stage, are not modeled in this work.

We typically find that tides on the star are the dominant sources of semimajor axis evolution (Jackson et al. 2008a, 2008b). When the eccentricity is large and damping, the tides on the planet can be the dominant semimajor axis damping source (Jackson et al. 2008a; Ibgui & Burrows 2009). After surveying our suite of systems, we find that tidal heating can usually provide sufficient energy to inflate planetary radii as large as observed, but we do not always find an evolutionary history where the radius, semimajor axis, eccentricity, and age all simultaneously fall within the observed error bars. Regardless, we find that tidal processes are an important aspect of planet evolution, particularly for hot Jupiter systems.

3. MODEL: IMPLEMENTATION

The Fortney et al. (2007) giant planet thermal evolution model has been coupled to the Jackson et al. (2008b) tidal evolution model. Therefore, the semimajor axis, eccentricity, and radius of the planet all evolve simultaneously. The tidal power is assumed to be deposited uniformly into the envelope of the planet. The planet structure model is assumed to be composed of four parts.

1. A 50% rock/50% ice core (by mass) with the ANEOS equations of state (Thompson 1990). The core does not participate in the thermal evolution of the planet, as in Fortney et al. (2007).
2. An H/He envelope with $Y = 0.27$, which uses the equation of state of Saumon et al. (1995). The envelope is assumed to be fully convective and thus has constant specific entropy throughout. At each time step, the envelope is assumed to be in hydrostatic equilibrium.
3. A series of radiative-convective, equilibrium chemistry, non-gray atmosphere models described in more detail in Fortney et al. (2007) and Fortney et al. (2008). These grids are computed for the incident fluxes at 0.02, 0.045, 0.1, and 1 AU from the Sun. This correctly determines the atmospheric structure and luminosity of the planet as a function of the planet's surface gravity, incident flux from the host star, and interior specific entropy. In cases, where the planet migrates to a semimajor axis with more incident flux than the innermost grid, the boundary condition at the innermost grid is used.
4. An extension of the atmosphere to a radius where the slant optical depth in a wide optical band (the *Kepler* bandpass) reaches unity. Therefore, all plotted radii are at the "transit radius," as discussed by several authors (Hubbard et al. 2001; Baraffe et al. 2003; Burrows et al. 2003). The slant optical depth as a function of pressure is computed with the code described in Hubbard et al. (2001) and Fortney et al. (2003). We have found that the atmosphere height

approximately follows the following relation

$$h = 10^{8.74} \frac{T_{\text{eff}}}{g}, \quad (1)$$

where h is the height in centimeter of the atmosphere from 1 kbar (approximately the depth where the radiative/convective zone boundary lies) to 1 mbar (where the planet becomes optically thin), g is the planet's surface gravity (cgs), and T_{eff} is the effective temperature in Kelvin. Taking into account this atmosphere height is significant when the planet has low gravity or high-effective temperature. In Fortney et al. (2007), the radii at 1 bar were presented.

The orbital-tidal evolution model is described in detail by Jackson et al. (2008b, 2009), and references therein. The equations used in this work are

$$\frac{1}{a} \frac{da}{dt} = - \left[\frac{63\sqrt{GM_s^3} R_p^5}{2Q'_p M_p} e^2 + \frac{9\sqrt{G/M_s} R_s^5 M_p}{2Q'_s} \left(1 + \frac{57}{4} e^2 \right) \right] a^{-13/2}, \quad (2)$$

$$\frac{1}{e} \frac{de}{dt} = - \left[\frac{63\sqrt{GM_s^3} R_p^5}{4Q'_p M_p} + \frac{225\sqrt{G/M_s} R_s^5 M_p}{16Q'_s} \right] a^{-13/2}, \quad (3)$$

$$P_t = \frac{63}{4} \left[(GM_s)^{3/2} \left(\frac{M_s R_p^5 e^2}{Q'_p} \right) \right] a^{-15/2}, \quad (4)$$

where a is the semimajor axis, e is the eccentricity, and P_t is the tidal power deposited into the planet. This model attempts to describe tidal heating only by orbit circularization and ignores other forms of tides such as spin synchronization or obliquity tides, which are not believed to be as important. This model assumes that the star is rotating slowly relative to the orbit of the planet and is second order in eccentricity. Therefore, the evolution histories that include periods when the orbit has high eccentricity should be regarded with caution. Because there is a lot of other uncertainty with regard to tidal theory, we choose to use this simple model instead of more complex models such as Wisdom (2008). For at least one of the 45 systems, HAT-P-2, the planet-star system may be able to achieve a double tidally locked equilibrium state (star is tidally locked to the planet and the planet is tidally locked to the star) as shown by Levrard et al. (2009); in this system it is not a good assumption that the star is rotating slower than the period of the orbit. However, Levrard et al. (2009) find that this assumption is valid for most stars. We find that tidal heating is largest where e is not particularly large ($\lesssim 0.4$ falling toward zero), so this theory suffices for our purposes. Q'_p is the tidal Q parameter of the planet and Q'_s is the tidal Q parameter of the star. In this work, we have predominantly investigated cases when $Q'_p = Q'_s = 10^5$ as well as the case of $Q'_p = 10^{6.5}$, $Q'_s = 10^5$. Since the Q value is in principle a function of the driving frequency (Ogilvie & Lin 2004), amplitude of the distortion, and internal structure of the body, the Q value for close in extra solar giant planets is potentially not equal to the Q value for Jupiter. If the Q value is a very "spiky" function of the driving frequency, then the system might spend a lot of time in a state where the tidal effects are occurring at a slow rate and quickly pass through states where tidal effects are rapid. The stellar Q value is typically estimated through the observed circularization of binary stars orbits, but

has also been estimated by modeling the dissipation inside of a star (Ogilvie & Lin 2007).

We assume that the tidal power is uniformly deposited into the envelope of the planet. The net energy loss is given by the following equation:

$$(L - P_t)\Delta t = \int T \Delta S dm, \quad (5)$$

where L is the luminosity at the planet's surface, Δt is some small nonzero time step, and S is the specific entropy. If $P_t > L$, then the planet's envelope will be increasing in entropy and the planet's radius will increase. More typically, $P_t < L$ and the planet's entropy is decreasing and thus the planet is contracting. The power ratio P_t/L is a useful measure of how important tidal effects are. It clearly indicates whether there is a net energy input (ratio larger than unity) or net energy loss (ratio smaller than unity).

For a given radius, assumed core size and average incident flux of the planet, $\dot{R}_p \propto -L_{\text{net}}$. Therefore, if we calculate R_{NH} , the radius contraction rate when there is no internal heat source, we can use the following relationship to calculate \dot{R}_p when there is an assumed P_t tidal heating (or an input power of another source).

$$\frac{\dot{R}}{R_{NH}} = \frac{L - P_t}{L}. \quad (6)$$

Due to tidal migration, the incident flux upon the planet increases with time. Based on the planet's incident flux at a given time, we interpolate in the four grids which include the incident flux level from the Sun at 0.02, 0.045, 0.1, and 1 AU. Here, we neglect the more minor effect that parent star spectra can differ somewhat from that of the Sun.

In order to examine all the plausible evolutionary tracks for each of the 45 transiting planets studied, we modeled their thermal evolution over a range of

1. initial semimajor axis: the observed semimajor axis to five times the observed value,
2. initial eccentricity: from 0 to 0.8,
3. core mass: 0, 10 M_{\oplus} , 30 M_{\oplus} , 100 M_{\oplus} . For very massive planets we also consider core masses of 300 and 1000 M_{\oplus} . Except for GJ 436b, HAT-P-11b, and HD 149026b, the core was required to be at most 70% of the mass of the planet. For GJ 436b, we sample up to 21 M_{\oplus} and for HAT-P-12, we sample up to 23 M_{\oplus} .

Each of these possible evolution histories were run until either (1) the time reached 14 Gyr, (2) the entropy of the envelope became larger or smaller than the range of entropy values in the grid of hydrostatic equilibrium structures, or (3) the planet reaches a small orbital distance $\sim R_s$ (realistically, the planet would be disrupted before this stage, but in this work we do not model the mass loss process).

For each run, we searched the evolution history during the estimated system age range for times when the orbital parameters were also within their observed range. If this occurred, we then recorded the transit radius during these times and compared the range of achieved values to observed values. In situations, where a good estimate on the age is not available, we searched within 1 to 5 Gyr. When a secondary eclipse constraint on the eccentricity is not available we assume that the eccentricity value is 0.025 ± 0.025 (i.e., the likely range is between 0 and 0.05, although we have recently learned that the actual uncertainties may be far larger; see Madhusudhan &

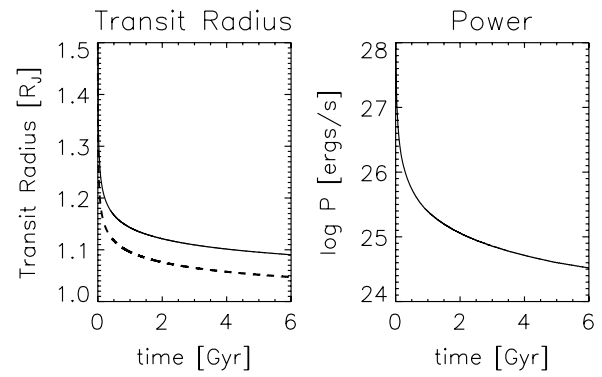


Figure 1. Radius and intrinsic planet luminosity evolution for a $1 M_J$ planet at 0.05 AU around a $1 M_{\odot}$ star without any tidal effects. In the left panel, the dashed line is the radius at 1 kbar, near the convective/radiative boundary at gigayear ages. The solid line is the radius where the atmosphere reaches 1 mbar—approximately the radius that would be observed in transit.

Winn 2009). In cases, where the eccentricity is observed to be consistent with zero from a secondary eclipse, we assume that the eccentricity value is 0.005 ± 0.005 (i.e., the likely range is between 0 and 0.01). We use the observed semimajor axis and error. We then search for instances of evolution histories during the possible age range that have an error-normalized distance less than 3 to the observed value. This distance is defined as

$$\sqrt{(a_i - a_m)^2 / \sigma_a^2 + (e_i - e_m)^2 / \sigma_e^2}, \quad (7)$$

where a_i and e_i are the orbital parameters for the instance of a particular run and a_m , σ_a , e_m , and σ_e are the measured/assumed semimajor axis, semimajor axis σ , eccentricity, and eccentricity σ . Planet orbital parameters, transit radii, and stellar parameters are from F. Pont's Web site at <http://www.inscience.ch/transits/> and The Extrasolar Planets Encyclopedia at <http://exoplanet.eu/>; please see the note added in proof.

4. GENERAL EXAMPLES

Here, we add different components of the model step-by-step, such that each effect can be appreciated independently. The two opposing effects of tidal evolution are late-time heating that is associated with eccentricity damping and more efficient early-time cooling due to initial semimajor axes that are larger than the present value. The four cases present are for a $1 M_J$ planet orbiting a $1 M_{\odot}$ star at 0.05 AU. In each of these cases, we assume that the planet has a $10 M_{\oplus}$ core.

Case 1: no tidal effects, Figure 1. In the left panel, the solid line is the planet transit radius and the dot-dashed line is the radius at 1 kbar (near the convective-radiative boundary). In the right panel, the intrinsic planet luminosity is plotted as a function of time. As the planet contracts, the luminosity of the planet significantly decreases. Without an internal heat source or semimajor axis evolution the planet's radius monotonically decreases with time.

Case 2: no orbital evolution, constant interior heating, in Figure 2. In this case, the net output power is the difference between the intrinsic luminosity and a constant interior heating source of unspecified origin. In these evolution runs, the planet stops contracting when the intrinsic luminosity is equal to the constant heating source. This is equivalent to when the ratio between the input power and the luminosity of the planet is equal to unity. The upper 3 evolution tracks (purple, cyan, and blue) all reach an equilibrium between the interior heating and

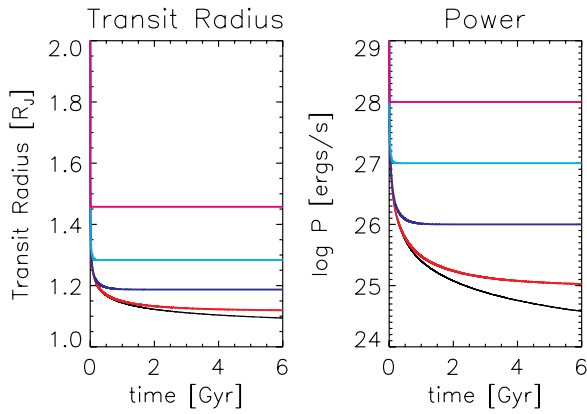


Figure 2. Same as Figure 1, but with various constant heating applied in the interior of the planet. Moving from bottom to top, the constant heating rates are 10^{24} , 10^{25} , 10^{26} , 10^{27} , and 10^{28} erg s $^{-1}$.

(A color version of this figure is available in the online journal.)

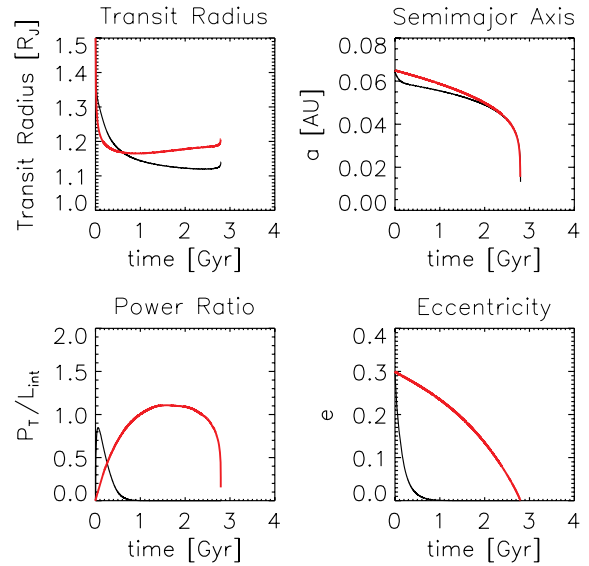


Figure 4. Coupled planet thermal evolution and orbital evolution. $Q'_p = 10^5$ and $Q'_p = 10^{6.5}$ cases both with $Q'_s = 10^5$ are plotted in black and red, respectively. We plot, the radius evolution in the upper left, semimajor axis evolution in the upper right, ratio between tidal heating and intrinsic planet luminosity in the lower left, and eccentricity in the lower right.

(A color version of this figure is available in the online journal.)

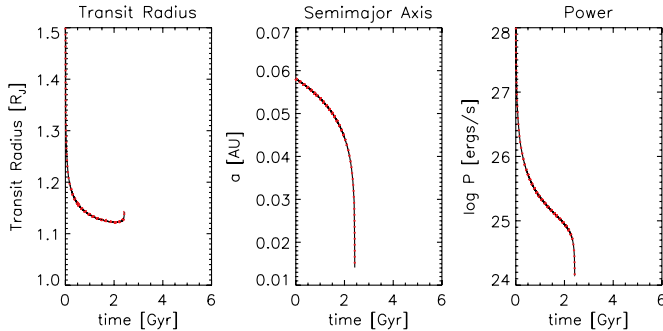


Figure 3. Planet thermal evolution with orbit evolution, but without tidal heating. Transit radius, semimajor axis and the planet's intrinsic luminosity are plotted from left to right. $Q'_p = 10^5$ and $Q'_p = 10^{6.5}$ cases are plotted in black and red, respectively.

(A color version of this figure is available in the online journal.)

luminosity of the planet within 2 Gyr, but the evolution runs with lower input power do not reach an equilibrium state in the 6 Gyr plotted. As expected, when there is more input power, the equilibrium radius is larger. In practice, the input power through tides or other processes will not be constant over gigayears, but a planet may be inflated to a radius such that it is in a temporary equilibrium state.

Case 3: tidal orbital evolution, but without tidal heating; Figure 3. This case demonstrates how the orbital evolution due to tides effects the thermal evolution of the planet. Here, we plot both the $Q'_p = 10^5$ (tidal effects on the planet occur faster) and $Q'_p = 10^{6.5}$ (tidal effects on the planet occur slower) cases with $Q'_s = 10^5$ in black and red, respectively. These curves track each other exactly because the tides on the planet do not significantly contribute to the migration when the eccentricity is small (here $e = 0$). When comparing Figure 1 to Figure 3, notice that in the second case, the power drops off more rapidly as the semimajor axis decreases. This is due to the increase in insolation by the parent star, which deepens the atmospheric radiative zone, lessening transport of energy from the interior (e.g., Guillot et al. 1996). Another result of moving the planet closer to the star is that there is an uptick in the transit radius. This is due only to an increase in the effective temperature, which increases the atmosphere height. The semimajor axis evolution accelerates as the planet moves inward due to the tidal migration rate's strong dependence on semimajor axis.

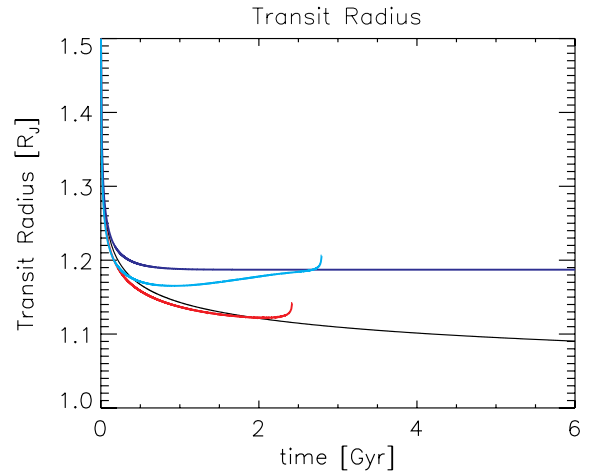


Figure 5. Radius evolution in different cases. Cases 1, 2, 3, 4 (see text) are plotted in black, blue, red, and cyan.

(A color version of this figure is available in the online journal.)

Case 4: tidal orbital evolution and tidal heating; Figure 4. We now put both the orbital evolution and corresponding tidal heating together. Black is the $Q'_p = 10^5$ case and red is $Q'_p = 10^{6.5}$ case. Notice that in the low Q'_p case, the planet circularizes quickly and tidal heating becomes less important. In the high Q'_p case, the planet is still undergoing circularization and significant tidal heating at late times. As a result, the radius in the high Q'_p case (slower rate of tidal effects in planet) can be larger than the low Q'_p case (faster rate of tidal effects in planet) at late times. Both trials start out with fairly modest eccentricity ($e = 0.3$).

In Figure 5, we compare the radius evolution in all four of these cases: Case 1 (no tidal effects, black), Case 2 (no orbital evolution, constant heating, blue), Case 3 (tidal orbital evolution, but not tidal heating, red), and Case 4 (full tidal evolution model, cyan). The cases with tidal evolution are plotted for the high Q'_p case. Clearly, when tidal heating is included (cyan or blue), it can

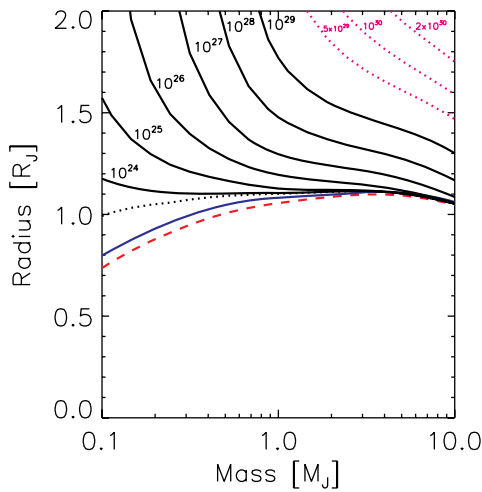


Figure 6. Dotted black line is the transit radius without any internal heating as a function of mass assuming a $10 M_{\oplus}$ core. In these models, we hold the planet at 0.05 AU around a $1 M_{\odot}$. The dashed red line is the 1 kbar radius—near the convective/radiative zone boundary. The blue line is the relation from Fortney et al. (2007). The solid black lines are the radius one would find if there were a constant heating source (values between 10^{24} and 10^{29} erg s $^{-1}$). The pink dotted lines were calculated in the same way, but required extrapolation (quadratic) off of the grid of atmosphere models.

(A color version of this figure is available in the online journal.)

result in a radius larger than achieved without including tidal heating (red or black). Since tidal heating is a time-varying quantity, the planet’s radius when tidal heating will not be as simple as in Case 2. Generally, the planet will experience significant tidal heating when the orbit is being circularized. At this time, the radius will increase, but after this time the radius of the planet will contract again. Also, because the planets in Case 3 (red) start at larger orbital distance than that of Case 1 (black), the radius contracts marginally faster when the planet is at larger semimajor axis. This is why the red line is lower than the black line before 2 Gyr. After this point, the transit radius increases in the red line case because the planet has moved close to the star, the effective temperature of the planet increases, and the atmosphere height also increases.

To examine how different levels of internal heating affect the radius of the planet, we plot the planet radius after 5 Gyr as a function of mass in Figure 6. Again, these models assume a $10 M_{\oplus}$ core, at a orbital distance of 0.05 AU around a $1 M_{\odot}$ star. In this figure, the black dotted line is the prediction of the thermal evolution model without tidal heating. The red dashed line is the base of the atmosphere at 1 kbar. Clearly, the height of the atmosphere is much larger for smaller planets due to their smaller gravities. The solid blue line is the radius relation from (Fortney et al. 2007). The solid black lines are the radius of the planet given a constant heating rate after 5 Gyr of evolution. The pink dotted curves are constructed in the same manner as the solid black curves, but required extrapolation (here, quadratic) off of the calculated atmosphere grid. At this point in time, most of these planets have reached an equilibrium state where an equal amount of internal heating is balanced by the planet’s intrinsic luminosity. Clearly, the effect on the radius for a given heating is larger for smaller mass planets.

5. RESULTS

5.1. Specific Systems

While we have computed the evolution history of 45 systems, here we show representative calculations for particular

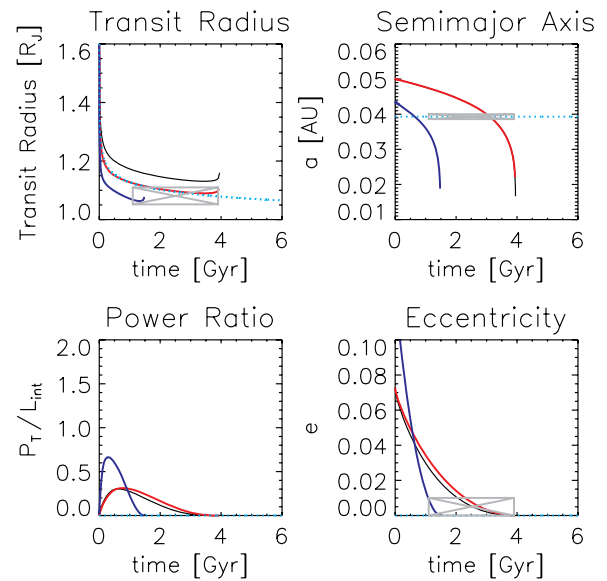


Figure 7. Possible tidal/thermal evolution tracks for the planet around the star TrES-1. Black: no core. Red: $10 M_{\oplus}$ core. Blue: $30 M_{\oplus}$ core. Cyan dotted: $10 M_{\oplus}$ core evolution history without tidal effects. This is a $0.76 M_J$ planet orbiting a $0.89 M_{\odot}$ star. Upper left panel: transit radius evolution. Upper right panel: semimajor axis evolution. Lower left panel: ratio between tidal power injected into the planet and intrinsic planet luminosity. Lower right panel: eccentricity evolution. Observed semimajor axis, eccentricity, and observed radius are plotted in their respective panels. These evolution tracks were selected to have orbital parameters that agree with the observed values. $Q'_p = 10^{6.5}$, $Q'_s = 10^5$.

(A color version of this figure is available in the online journal.)

samples of planets. These are TrES-1b, XO-4b, HD 209458b, and WASP-12b, and are shown in Figures 7, 8, 10, and 11, respectively. These four cases demonstrate qualitatively different cases. TrES-1b is a circularized planet with a “normal” radius value. XO-4b, HD 209458b, and WASP-12b are large-radius planets with a small relatively unconstrained eccentricity, zero eccentricity, and a nonzero value, respectively. In Figures 7–11, the transit radius evolution is plotted in the upper left panel, the semimajor axis evolution is plotted in the upper right panel, the ratio between the tidal power and luminosity is plotted in the lower left panel, and the eccentricity evolution is plotted in the lower right panel. The observed semimajor axis, eccentricity, and transit radius are plotted on each of the respective panels. The power ratio, tidal power to luminosity, describes how important tidal effects are to the energy flow of the planet. When this ratio is somewhat smaller than unity, tidal heating is relatively unimportant for the thermal evolution of the planet and when this ratio reaches or surpasses unity, tidal heating plays a more significant role in the thermal evolution. In each of these figures, a set of runs were selected such that the orbital parameters and transit radius are closest to the observed values.

TrES-1b is a transiting hot-Jupiter planet with zero or small eccentricity and a typical radius observation. The system is composed of a $0.76 M_J$ planet orbiting a $0.89 M_{\odot}$ star with a 0.04 AU semimajor axis. Tidal heating is not necessary to invoke to explain this system; we demonstrate that this tidal model can still explain these kinds of modest radius systems. Possible evolution histories with tidal effects are shown in Figure 7. These possible histories are selected such that their orbital parameters at the current age agree with the observed values and the transit radius that is close to the observed value. We show various core sizes in different colors: black for zero core, red for a $10 M_{\oplus}$

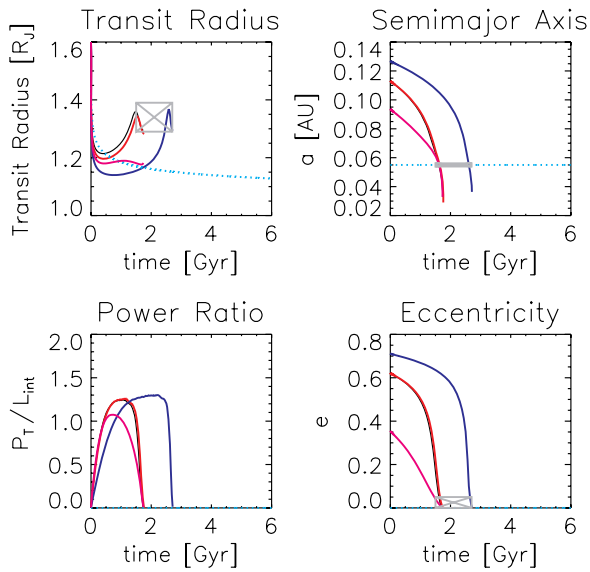


Figure 8. Possible tidal evolution tracks for the planet around the star XO-4. This is a $1.72 M_J$ planet orbiting a $1.32 M_\odot$ star. Black: no core. Red: $10 M_\oplus$ core. Blue: $30 M_\oplus$ core. Magenta: $30 M_\oplus$ core with a low initial eccentricity. Cyan dotted: $10 M_\oplus$ evolution history without tidal effects. Panels are analogous to Figure 7. The eccentricity that is marked in the lower right panel is our assumed possible range (0 to 0.05). These evolution tracks were selected to have orbital parameters that agree with the observed values. $Q'_p = Q'_s = 10^5$. Notice that the tidal models initially have smaller radii than the nontidal model because the tidal models are able to more efficiently cool at early times due to their larger semimajor axis.

(A color version of this figure is available in the online journal.)

core, and blue for a $30 M_\oplus$ core. The cyan dotted line is the evolution history of a nontidal thermal evolution model with a $10 M_\oplus$ core. Notice, the radius evolution of the nontidal model does not differ significantly from the radius evolution of the corresponding $10 M_\oplus$ (red) tidal model. In these possible evolution histories with tidal effects, the initial eccentricity is relatively small and tidal heating does not dominate the energy flux budget (in the lower left panel, the power ratio is always less than 1). However, the orbit decays significantly due to tides raised on the star by the planet, which continues even at $e = 0$. These tides cause these planet to migrate from an initial semimajor axis of 0.05 AU to 0.04 AU with the assumed $Q'_s = 10^5$. Figure 7 demonstrates that this model easily explains the radius of TrES-1b with a core between $10 M_\oplus$ and $30 M_\oplus$.

There is a slight upturn in radius just before an age of 4 Gyr. This is due to the heating of the planet's atmosphere at very small semimajor axis, and is *not* due to tidal power. As the planet reaches smaller orbital distances the incident flux it intercepts increases dramatically, leading to an enlarged atmospheric extension, and greater transit radius. This feature is also present in the recent paper by Ibgui & Burrows (2009). The tracks end when we stop following the evolution, with the assumption that the planet is disrupted or collides with the parent star. This is merely the first of many evolution tracks that we present with the end state being the disruption of the planet. This finding is essentially quite similar to that of Levrard et al. (2009) who find that all of the known transiting planets, save HAT-P-2b, will eventually collide with their parent stars. Robust observational evidence for this mechanism was recently detailed by Jackson et al. (2009).

XO-4b is an inflated planet where the eccentricity has not been well constrained, due to sparse radial velocity sampling (McCullough et al. 2008). In these cases, we search for instances

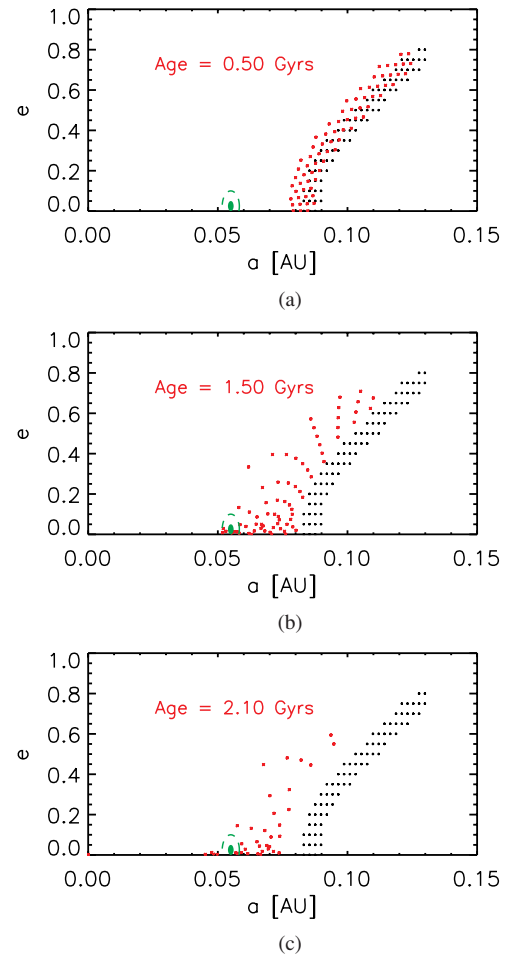


Figure 9. Grid of evolution histories for XO-4b that were found to be consistent with the orbital parameters at a later time. These histories are not required to also have a radius value that is consistent with the observed value. These evolution runs assume a core size of $10 M_\oplus$, $Q'_p = 10^5$, and $Q'_s = 10^5$. This serves as a sample for the type of calculation that was performed for every planet. Black: original orbital parameters of each run. Red: orbital parameters at a later marked time (0.5 Gyr, 1.5 Gyr, and 2.1 Gyr). The filled green circle is the 1σ zone, while the dashed region is the 3σ zone.

(A color version of this figure is available in the online journal.)

over the evolution histories where the eccentricity is between 0 and 0.05, because we assume that a larger value would have been clearly noticed in radial velocity data. With this eccentricity constraint, we show in Figure 8 that there is a narrow period of time when we can explain the inflated state with a recent circularization of the orbit that has deposited energy into the interior of the planet. The evolution curves shown here are for tidal parameters $Q'_p = 10^5$ and $Q'_s = 10^5$; in the higher Q'_p case, the radius evolution curves do not agree with the observed value. In Figure 8, we show black, red, and blue curves for evolution runs with no core, $10 M_\oplus$ core, and $30 M_\oplus$ core, respectively. The pink curve is an evolution history for low initial eccentricity with a $30 M_\oplus$ core. Again, the cyan curve is a no-tidal evolution history with $10 M_\oplus$ core. Since tidal power is deposited mainly when the planet is being circularized, *high initial eccentricity orbits are required for these planets to experience significant later tidal inflation*. Another interesting feature of this plot, is that when comparing the radius of the runs for different cores at any given time, we find that the radius is not always monotonically decreasing with core size. This shows

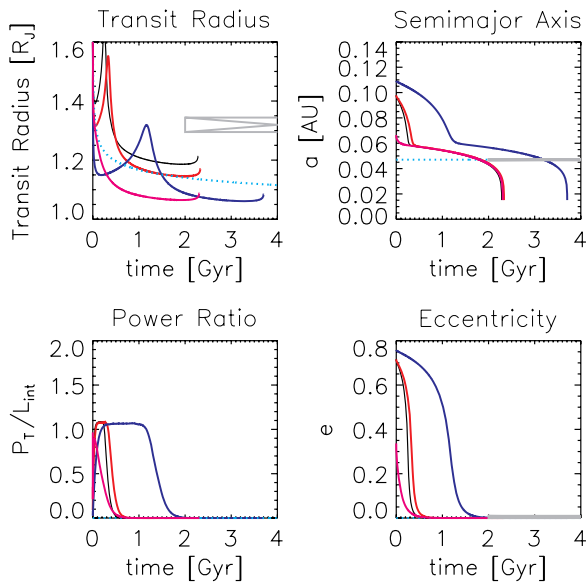


Figure 10. Possible tidal/thermal evolution tracks for the planet around the star HD 209458. This is a $0.657 M_J$ planet orbiting a $1.101 M_\odot$ star. The planet has a radius of $1.32 R_J$ and an observed eccentricity of zero. Black: no core. Red: $10 M_\oplus$ core. Blue: $30 M_\oplus$ core. Purple: $30 M_\oplus$ core with low initial eccentricity. Cyan dotted: $10 M_\oplus$ core evolution model without tidal effects. Panels are analogous to Figure 7. $Q'_p = Q'_s = 10^5$.

(A color version of this figure is available in the online journal.)

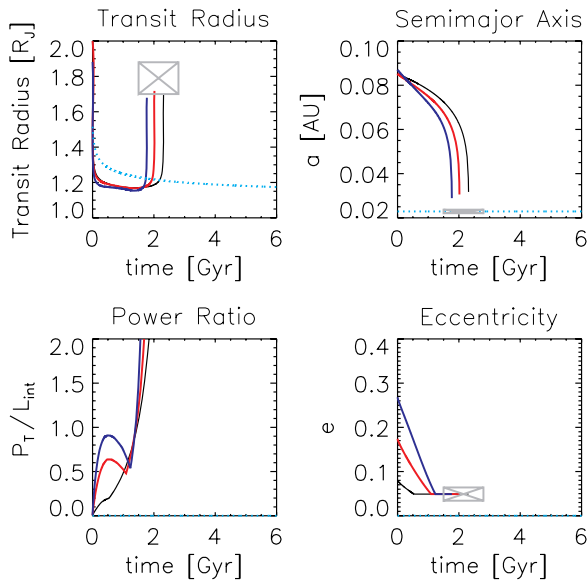


Figure 11. Possible tidal/thermal evolution for WASP-12b. This is a $1.41 M_J$ planet orbiting a $1.35 M_\odot$ star. The planet has a very large observed transit radius of $1.79 R_J$ and an eccentricity of 0.05. In these evolution histories, we impose an eccentricity floor mimicking the effects of an eccentricity driving force. Black: no core. Red: $10 M_\oplus$ core. Blue: $30 M_\oplus$ core. Cyan dotted: $10 M_\oplus$ core evolution history without tidal effects. Panels are analogous to Figure 7. $Q'_p = 10^5$ and $Q'_s = 10^5$.

(A color version of this figure is available in the online journal.)

that uncertain past orbital–tidal history can lead to uncertainty in derived structural parameters such as the core mass.

As an example of the kind of calculation that was performed for every planet, in Figure 9, we show snapshots of the orbital parameters (a and e) of the ensemble of systems that are at some point consistent with the observed orbital parameters

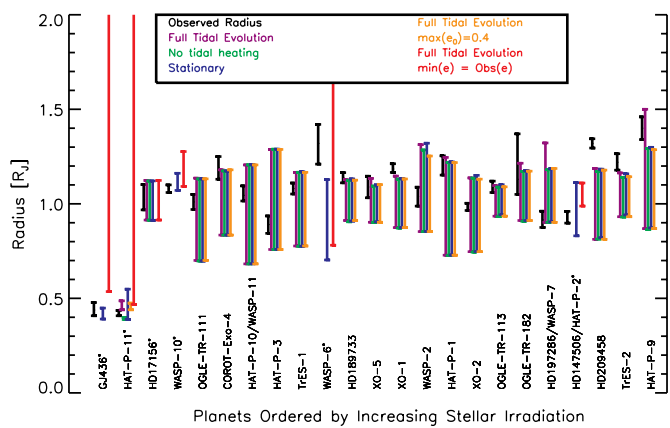
and age of XO-4b. Note that we do not require that the radius simultaneously also agree with the observed radius, but rather compare the range of possible radius values achieved by the model to the actual observed value. The black points are the original orbital parameters. The red points are the orbital parameters for one of these runs at a later point in time (0.5 Gyr, 1.5 Gyr, and 2.1 Gyr). The filled green circle marks the 1σ observed orbital parameters, while the dashed region is the 3σ zone.

HD 2094598b is a large-radius planet with eccentricity that has been observed to be very close to zero (Deming et al. 2005). The planet is observed to have a radius of $1.32 R_J$ and mass of $0.657 M_J$. Therefore, we require evolution histories for this system are shown in Figure 10 with $Q'_p = 10^5$ and $Q'_s = 10^5$. With these chosen Q values, we find that the planet could have experienced tidal heating at a previous time, however by the time it has an eccentricity of 0.01 or less the planet’s radius has since deflated below the observed value. It is possible to find an evolution histories that agrees with the observations by allowing different Q values, as shown by Ibgui & Burrows (2009). Although the tidal Q value is not strongly constrained and may even vary depending on the configuration of the system (Ogilvie & Lin 2004), it is our view that it makes the most sense to fix the Q value close to prior inferred values. Again, the black, red, and blue curves correspond to no core, $10 M_\oplus$ core, and $30 M_\oplus$ core sizes, respectively. The cyan curve is a nontidal thermal evolution history for a $10 M_\oplus$ core. In these cases, tidal power is sufficient to inflate the planet’s radius to its observed value, however, we do not find evolution histories that also agrees with the other observed parameters—especially the eccentricity. In the semimajor axis evolution, there is a clear transition knee where the rate of orbital evolution decreases. The first phase is due to tidal effects of both the star and planet while the eccentricity is nonzero. The second phase is mainly due to tides on the star when the eccentricity is zero.

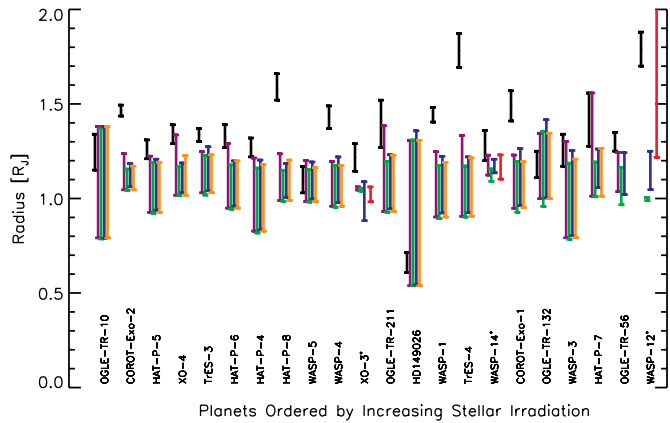
WASP-12b is a planet with an especially large radius of $1.79 R_J$ with a nonzero eccentricity of 0.05 (Hebb et al. 2009). An interesting property of this system is that the planet is filling at least 80% of its Roche lobe by radius (Li et al. 2009). Figure 11 shows evolution curves in black, red, and blue for no core, $10 M_\oplus$ core, and $30 M_\oplus$ core cases, respectively when an eccentricity floor is imposed. The thermal evolution without tidal evolution is shown in cyan. In these tidal cases, the tidal power increases in strength as the semimajor axis decays until the planet undergoes a rapid expansion. When the semimajor axis gets small enough, the tidal power exceeds the luminosity and the planet’s radius rapidly increases. This happens both because the incident flux decreases the intrinsic luminosity of the planet and tidal heating has a strong semimajor axis dependence ($P_t \sim a^{-15/2}$). We do not model the mass loss process, which is likely to occur at late times for systems such as these (Gu et al. 2003) This should only be taken as evidence that if there was an eccentricity driving companion similar to mechanisms suggested by Mardling (2007), then it may be possible to heat this planet to quite large radii.

5.2. Summary for Suite

We have summarized our results for all 45 planetary systems in Figures 12 and 13 for Q'_p equal to 10^5 and $10^{6.5}$. In these figures, we have plotted the observed radius range (lower limit to upper limit) in black. The achieved radius range under various assumptions is plotted in color. Possible radii are recorded in



(a)



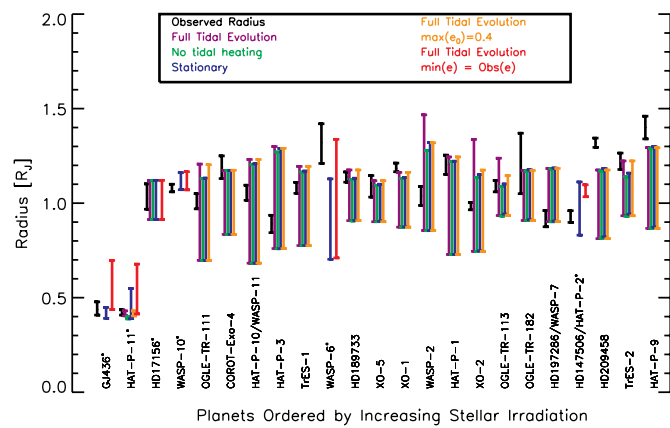
(b)

Figure 12. Observed planet radius (black) compared to a range of achieved model radii (colors) using $Q'_p = 10^5$; $Q'_s = 10^5$. Planets are ordered by increasing incident flux according to their current observed eccentricities. Planets are marked with a * if they have nonzero observed eccentricity. The range of possible radius values under the full tidal evolution model is plotted in purple with initial eccentricity between 0 and 0.8. The radius range for a model with tidal-orbital evolution, but without the tidal heating into the interior of the planet is plotted in green. The radius range for a standard stationary model without any tidal effects is plotted in blue. The radius range for the full tidal evolution model with a maximum initial eccentricity of 0.4 is plotted in orange. In cases, where a nonzero eccentricity has been observed, the radius range with an eccentricity floor equal to the observed value is shown in red.

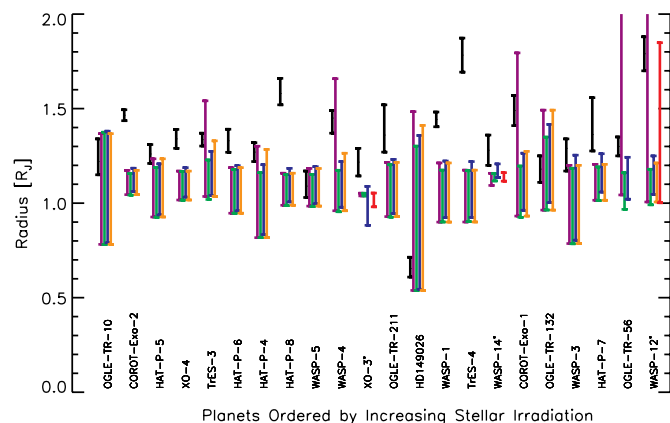
(A color version of this figure is available in the online journal.)

instances of the evolution histories when the orbital parameters and age all agree with the observed a , e , and age values (as defined previously, within three error-normalized distance units of the observed value). The age of each system is often quite uncertain; since the possible radius values are sensitive to the age of the system, this is a large source of uncertainty for our results. For each planet, a range of radius values is plotted for up to five different successful types of models. These are models computed as discussed in Section 4.

1. The full tidal evolution model is shown in purple. In this model, the initial eccentricity was sampled from 0 to 0.8 and the initial semimajor axis was sampled from the observed semimajor axis to $5 \times$ the observed value. This is Case 4 in Section 4.
2. The model with tidal migration but without heating is shown in green. We perform the same search procedure as in the full tidal model. This model is not meant to be physical, but to give us an understanding of how tidal orbital migration alone affects the planet's radius. This is Case 3 in Section 4.



(a)



(b)

Figure 13. Observed planet radius (black) compared to a range of viable model radii (colors) using $Q'_p = 10^{6.5}$; $Q'_s = 10^5$. Qualitatively, we observe the same trends that were observed in Figures 12(a) and (b). A larger Q'_p value decreases the rate of tidal effects via tides on the planet. Typically the tides on the planet from the star are responsible for circularizing the orbit, while tides on the planet from the planet are responsible for decreasing the semi-major axis. In the larger Q'_p case, the tidal circularization can be delayed for longer, which can make the possible radius of the planet larger. On the other hand, a larger Q'_p also decreases the power deposited into the planet.

(A color version of this figure is available in the online journal.)

3. The “stationary” model is shown in blue with all tidal effects turned off. These are “standard” cooling/contraction models, quite similar to those in Fortney et al. (2007). These models differ slightly than the models listed in Fortney et al. (2007) in two ways. First, these models more accurately take into account the height of the atmosphere. Second, some of these models explore a wider range of core sizes. This is Case 1 in Section 4.
4. For planets, whose current observed eccentricity is less than 0.4, the full tidal evolution with an maximum initial eccentricity of 0.4 is plotted in orange. Because tidal heating in the planet is directly connected to eccentricity damping, these runs serve as a demonstration of relatively less tidal heating due to circularization. This is a subset of Case 4 from Section 4.
5. For systems, where there is a measured nonzero eccentricity, we simulate the effects of an eccentricity source by performing the full tidal evolution with an eccentricity floor equal to the observed value. These cases are shown in red. This is essentially a combination of Case 4 and Case 2.

Table 1
Model Calculations for Selected Transiting Systems

System	Core [M_E]	Radius Range ($Q'_p = 10^5$)	Radius Range ($Q'_p = 10^{6.5}$)	P (erg s $^{-1}$)	\dot{R}_{NH} (R_J yr $^{-1}$)
HD209458				$C_T = 6.3 \times 10^{25}$	
$M_p = 0.69 M_J$	0.0	1.12–1.19	1.13–1.18	$L = 1.5 \times 10^{26}$	-4.2×10^{-7}
$R_p = 1.32 R_J$	10.0	1.08–1.15	1.08–1.15	$L = 3.8 \times 10^{26}$	$-1. \times 10^{-6}$
$a = 0.05$ AU	30.0	1.02–1.08	1.02–1.07	$L = 1.6 \times 10^{27}$	-4.5×10^{-6}
$e = 0.00$	100.0	0.81–0.90	0.81–0.84	$L = 7.6 \times 10^{28}$	-1.5×10^{-4}
COROT-Exo-1				$C_T = 9.2 \times 10^{27}$	
$M_p = 1.03 M_J$	0.0	1.14–1.23	1.16–1.79	$L = 1.2 \times 10^{27}$	-2.2×10^{-6}
$R_p = 1.49 R_J$	10.0	1.11–1.21	1.13–1.79	$L = 1.8 \times 10^{27}$	-3.3×10^{-6}
$a = 0.03$ AU	30.0	1.07–1.15	1.08–1.52	$L = 3.8 \times 10^{27}$	-7.3×10^{-6}
$e = 0.00$	100.0	0.95–1.03	0.93–1.07	$L = 5.3 \times 10^{28}$	$-1. \times 10^{-4}$
COROT-Exo-2				$C_T = 3.8 \times 10^{27}$	
$M_p = 3.31 M_J$	0.0	1.11–1.23	1.11–1.17	$L = 6.1 \times 10^{28}$	-1.4×10^{-5}
$R_p = 1.47 R_J$	10.0	1.11–1.24	1.11–1.16	$L = 7.0 \times 10^{28}$	-1.6×10^{-5}
$a = 0.03$ AU	30.0	1.09–1.23	1.09–1.15	$L = 8.7 \times 10^{28}$	$-2. \times 10^{-5}$
$e = 0.00$	100.0	1.05–1.20	1.05–1.10	$L = 1.6 \times 10^{29}$	-3.9×10^{-5}
XO-4				$C_T = 3.3 \times 10^{25}$	
$M_p = 1.72 M_J$	0.0	1.15–1.34	1.15–1.17	$L = 1.7 \times 10^{27}$	-8.9×10^{-7}
$R_p = 1.34 R_J$	10.0	1.14–1.30	1.13–1.15	$L = 2.4 \times 10^{27}$	-1.2×10^{-6}
$a = 0.06$ AU	30.0	1.11–1.25	1.10–1.13	$L = 4.2 \times 10^{27}$	-2.2×10^{-6}
$e = 0.00$	100.0	1.02–1.11	1.02–1.03	$L = 3.2 \times 10^{28}$	-1.9×10^{-5}
HAT-P-6				$C_T = 4.3 \times 10^{25}$	
$M_p = 1.06 M_J$	0.0	1.16–1.29	1.16–1.19	$L = 4.2 \times 10^{26}$	-4.7×10^{-7}
$R_p = 1.33 R_J$	10.0	1.14–1.28	1.13–1.16	$L = 7.2 \times 10^{26}$	-8.3×10^{-7}
$a = 0.05$ AU	30.0	1.09–1.28	1.09–1.11	$L = 1.7 \times 10^{27}$	-2.1×10^{-6}
$e = 0.00$	100.0	0.95–1.09	0.95–0.96	$L = 3.2 \times 10^{28}$	-4.7×10^{-5}
HAT-P-7				$C_T = 8.0 \times 10^{26}$	
$M_p = 1.78 M_J$	0.0	1.14–1.55	1.14–1.21	$L = 6.3 \times 10^{26}$	-3.2×10^{-7}
$R_p = 1.36 R_J$	10.0	1.13–1.56	1.12–1.19	$L = 8.3 \times 10^{26}$	-4.3×10^{-7}
$a = 0.04$ AU	30.0	1.11–1.50	1.10–1.16	$L = 1.4 \times 10^{27}$	-7.3×10^{-7}
$e = 0.00$	100.0	1.01–1.44	1.02–1.06	$L = 6.8 \times 10^{27}$	-4.2×10^{-6}
HAT-P-9				$C_T = 5.0 \times 10^{25}$	
$M_p = 0.78 M_J$	0.0	1.16–1.49	1.16–1.29	$L = 7.0 \times 10^{26}$	-1.7×10^{-6}
$R_p = 1.40 R_J$	10.0	1.13–1.50	1.13–1.25	$L = 1.3 \times 10^{27}$	-3.3×10^{-6}
$a = 0.05$ AU	30.0	1.06–1.36	1.06–1.17	$L = 3.7 \times 10^{27}$	$-1. \times 10^{-5}$
$e = 0.00$	100.0	0.87–1.00	0.87–0.95	$L = 8.6 \times 10^{28}$	-1.7×10^{-4}
TrES-4				$C_T = 3.9 \times 10^{26}$	
$M_p = 0.93 M_J$	0.0	1.15–1.33	1.14–1.17	$L = 1.0 \times 10^{28}$	-4.4×10^{-5}
$R_p = 1.78 R_J$	10.0	1.12–1.32	1.11–1.14	$L = 1.4 \times 10^{28}$	$-6. \times 10^{-5}$
$a = 0.05$ AU	30.0	1.07–1.29	1.06–1.09	$L = 3.4 \times 10^{28}$	-1.2×10^{-4}
$e = 0.00$	100.0	0.91–0.99	0.90–0.92
OGLE-TR-211				$C_T = 6.4 \times 10^{25}$	
$M_p = 1.03 M_J$	0.0	1.14–1.38	1.14–1.22	$L = 5.0 \times 10^{26}$	-6.7×10^{-7}
$R_p = 1.36 R_J$	10.0	1.12–1.36	1.12–1.19	$L = 8.2 \times 10^{26}$	-1.1×10^{-6}
$a = 0.05$ AU	30.0	1.08–1.38	1.07–1.13	$L = 1.9 \times 10^{27}$	-2.7×10^{-6}
$e = 0.00$	100.0	0.93–1.10	0.93–0.97	$L = 3.6 \times 10^{28}$	-5.8×10^{-5}
WASP-1				$C_T = 5.2 \times 10^{26}$	
$M_p = 0.87 M_J$	0.0	1.16–1.25	1.16–1.21	$L = 6.1 \times 10^{26}$	-1.4×10^{-6}
$R_p = 1.44 R_J$	10.0	1.13–1.22	1.13–1.18	$L = 1.0 \times 10^{27}$	-2.4×10^{-6}
$a = 0.04$ AU	30.0	1.07–1.18	1.07–1.10	$L = 2.4 \times 10^{27}$	-6.2×10^{-6}
$e = 0.00$	100.0	0.90–1.06	0.90–0.92	$L = 5.1 \times 10^{28}$	-1.2×10^{-4}
WASP-4				$C_T = 1.3 \times 10^{28}$	
$M_p = 1.27 M_J$	0.0	1.12–1.20	1.13–1.66	$L = 3.3 \times 10^{27}$	-3.8×10^{-6}
$R_p = 1.45 R_J$	10.0	1.11–1.18	1.10–1.51	$L = 4.6 \times 10^{27}$	-5.4×10^{-6}
$a = 0.02$ AU	30.0	1.07–1.11	1.08–1.52	$L = 8.2 \times 10^{27}$	$-1. \times 10^{-5}$
$e = 0.00$	100.0	0.96–1.03	0.96–1.18	$L = 7.5 \times 10^{28}$	-8.7×10^{-5}

Table 1
(Continued)

System	Core [M_E]	Radius Range ($Q'_p = 10^5$)	Radius Range ($Q'_p = 10^{6.5}$)	P (erg s $^{-1}$)	\dot{R}_{NH} (R_J yr $^{-1}$)
WASP-12				$C_T = 1.1 \times 10^{29}$	
$M_p = 1.41 M_J$	0.0	...	1.18–2.02	$L = 2.5 \times 10^{28}$	-5.2×10^{-5}
$R_p = 1.79 R_J$	10.0	...	1.16–1.57	$L = 3.6 \times 10^{28}$	$-7. \times 10^{-5}$
$a = 0.02$ AU	30.0	...	1.12–1.37	$L = 5.9 \times 10^{28}$	-1.1×10^{-4}
$e = 0.05$	100.0	...	1.01–1.11

Notes. Various large-radius hot Jupiter planets have been listed. In the first column, we list the observed parameters of the system for reference. In the second column, we list an assumed core size. The achieved radius range for two different Q'_p values is listed in the third and fourth columns. In the fifth column, we list relevant power quantities. The coefficient of tidal power is listed in the first row for each system. In the following rows, we list the luminosity of the planet for the assumed core mass. In the final row, we calculate \dot{R}_{NH} , the radius derivative when there is no internal heating source.

Table 2
Model Calculations for Selected Transiting Systems

System	Core [M_E]	Radius [R_J] (5,6)	Radius [R_J] (5,7)	Radius [R_J] (6,5,6)	Radius [R_J] (6,5,7)
HD 209458					
$M_p = 0.69 M_J$	0.0	1.12–1.19 (683)	1.12–1.18 (737)	1.15–1.32 (816)	1.15–1.31 (1036)
$R_p = 1.32 R_J$	10.0	1.09–1.16 (931)	1.09–1.15 (1136)	1.12–1.27 (765)	1.11–1.25 (945)
TrES-4					
$M_p = 0.93 M_J$	0.0	1.16–1.22 (1291)	1.16–1.21 (849)	1.24–1.43 (665)	1.19–1.37 (1205)
$R_p = 1.78 R_J$	10.0	1.13–1.19 (1285)	1.13–1.18 (959)	1.20–1.37 (512)	1.16–1.33 (1154)
HAT-P-8					
$M_p = 1.52 M_J$	0.0	1.15–1.19 (1520)	1.15–1.19 (1390)	1.17–1.28 (538)	1.18–1.30 (728)
$R_p = 1.58 R_J$	10.0	1.13–1.18 (1515)	1.13–1.18 (1390)	1.16–1.26 (501)	1.17–1.28 (694)
WASP-1					
$M_p = 0.87 M_J$	0.0	1.17–1.21 (835)	1.17–1.20 (26)	1.23–1.48 (656)	1.19–1.39 (1463)
$R_p = 1.44 R_J$	10.0	1.14–1.18 (829)	1.14–1.17 (297)	1.20–1.45 (636)	1.16–1.35 (1438)
COROT-Exo-2					
$M_p = 3.31 M_J$	0.0	1.12–1.18 (1337)	1.12–1.19 (1069)	1.19–1.40 (1243)	1.13–1.33 (2127)
$R_p = 1.47 R_J$	10.0	1.11–1.17 (1334)	1.11–1.19 (1092)	1.18–1.39 (1242)	1.12–1.32 (2120)

Notes. Achieved radius values for 5 systems with high Q'_s for core size 0.0 and $10 M_\oplus$. The parameters used are denoted in the header with ($\log Q'_p \log Q'_s$). In the body of the table, the range or achieved radius values is listed along with the number of runs found in parenthesis.

For some planets, some of these ‘Cases’ were either not possible to compute or in no instances were the observed parameters consistent with the model parameters. For instance, in cases when the observed eccentricity is larger than 0.4, the tidal evolution histories with 0.4 maximum initial eccentricity are never consistent with the observation. In these cases, no radius range is drawn. In some of the cases, where tidal heating is included, an evolution history is found where a large amount of energy is deposited into the planet while the orbital parameters are consistent with observations. These result in a maximum achieved radius that sometimes exceeds $2 R_J$. In some of these cases, the planet will later cool off before the evolution stops. In other cases, the tidal power is sufficient to increase the planet’s entropy beyond the maximum entropy of our grid, which ends the evolutionary calculation. In the future, we plan to include mass loss and the subsequent evolution history.

By comparing these models we find a few interesting patterns. When comparing the full tidal evolution model (purple) to the stationary model (blue), notice that there are some cases where the full tidal model has a larger maximum radius and other cases where the reverse is true. This can be understood to be caused by the two competing effects of tidal evolution. Tidal heating puts power into the planet and inflates the radius, and tidal orbital evolution allows the planet to cool more efficiently at earlier times when the planet is less irradiated by the parent star. It is also useful to compare these two cases to the no heating model.

The no heating model generally has a smaller maximum radius than the stationary model because of the second effect. The tidal model has a larger maximum radius than the no heating model because of energy deposition into the planet.

Often the model achieves large radius values through a recent circularization of an originally high eccentricity orbit. During the circularization event (when the eccentricity drops significantly), tidal dissipation in the interior of the planet may deposit sufficient energy to significantly inflate the planet. The orange case (maximum initial eccentricity equal to 0.4) has been plotted to compare against the purple (initial eccentricity up to 0.8) to show how large initial eccentricity evolution histories contribute to the maximum achieved radius. Note that in the low Q'_p case in Figure 12, extremely large radii can be achieved for GJ 436b and HAT-P-11. This happens in our model through a recent rapid circularization of the orbit.

It may also be possible to have tidal heating without large initial eccentricities if there is a eccentricity driving source in the system. In some cases, such as in WASP-6b or WASP-12b, the resulting tidal heating may be enough to explain the large transit radius. By comparing red (tidal evolution with an eccentricity floor) to the purple (regular tidal evolution), larger radius values can be achieved when the orbit is not allowed to circularize.

Tidal evolution and heating clearly have important effects on a planet’s evolution, but not all of the large-radius planets could be explained through this mechanism, given our chosen Q

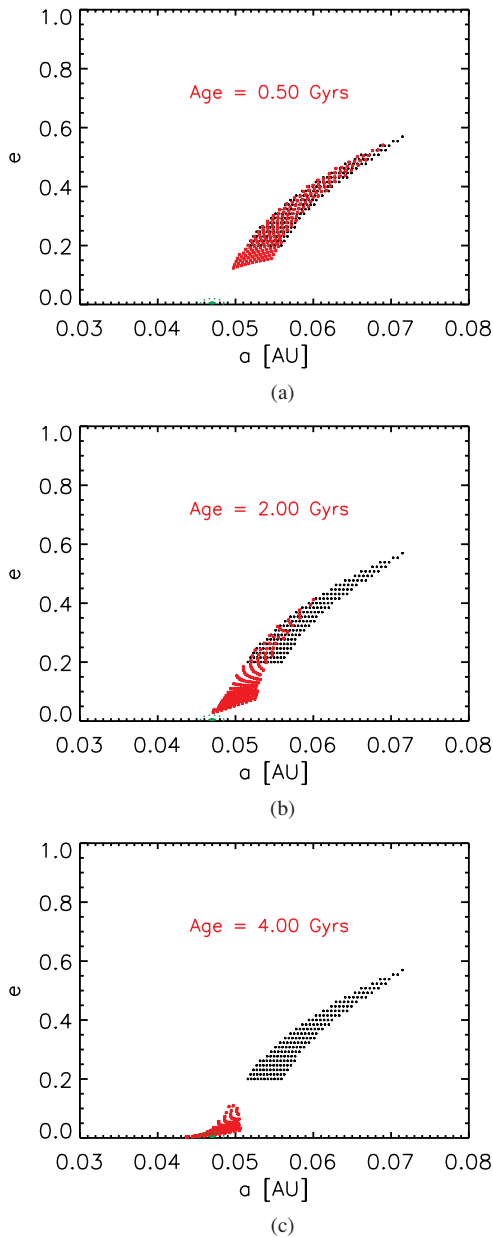


Figure 14. Grid of evolution histories (with initial $e > 0.2$) that were found to be consistent with the orbital parameters at a later time for the system HD 209458. These evolution runs assume there is no core, $Q'_p = 10^{6.5}$ and $Q'_s = 10^6$. Black: original orbital parameters of each run. Red: orbital parameters at a later marked time (0.5 Gyr, 1.5 Gyr, and 2.1 Gyr). The filled green circle is the 1σ zone, while the dashed region is the 3σ zone.

(A color version of this figure is available in the online journal.)

values. The planets HD 209458b, COROT-EXO-2b, HAT-P-9b, WASP-1b, and TrES-4b have radii that are larger than achieved in our models in both the low and high Q'_p cases. Typically, while it is possible to inflate the radius to the observed values, it difficult to find the system with an inflated radius and low current eccentricity. WASP-12b was explained if we assume that its eccentricity is maintained.

When comparing Figure 12 to Figure 13, it is interesting that some of the planets that are not explainable in the lower Q'_p case can be explained with larger Q'_p . Although $Q'_p = 10^5$ results in tidal heating being stronger than the $Q'_p = 10^{6.5}$ case, it also results in circularization on a shorter timescale.

In the $Q'_p = 10^{6.5}$ cases, it is often common for there to be a possible recent circularization of a high-initial eccentricity orbit where no such history was found in the $Q'_p = 10^5$ evolution runs.

In Table 1, we have selected a set of the largest planets and listed various properties. In the left column, we list the observed parameters. For various core sizes, we list the achieved radius of the tidal model in the low Q'_p and high Q'_p cases, the estimated luminosity of the planet at its current radius, and the current contraction rate of the planet without internal heating (previously defined as R_{NH}). Also, on the top row for each planet, we list the coefficient of tidal heating. This is defined as

$$C_T \equiv \frac{P_T}{\left(\frac{e}{0.01}\right)^2 \left(\frac{10^5}{Q'_p}\right)} \quad (8)$$

$$= \frac{63}{4} (GM_*)^{3/2} M_* R_p^5 a^{-15/2} \times 10^{-9}. \quad (9)$$

This quantity allows one to get an order-of-magnitude idea of recent tidal heating given the more constrained properties of the system (radius of the planet, masses of the bodies, and semimajor axis). The actual tidal power will greatly depend on the eccentricity and Q values, which are more uncertain. The ratio between the luminosity of the planet and this coefficient of tidal heating is a dimensionless number that describes how important tidal effects can be for a given core size. Certainly, since $P_T \propto e^2$ and Q'_p is quite uncertain, this ratio is not a strong test of tidal effects, but it is a simple way of testing how important tidal effects presently can be. Notice also that for an assumed tidal power, we can compute the present contraction rate using this table and Equation (6).

When calculating the contraction rate, the planet is assumed to be located at the current observed semimajor axis, which determines the incident flux from the star, structure of the planet's atmosphere, and thus the intrinsic luminosity of the planet at each time. For these large-radius systems, the contraction rate is often very fast. If we assume that tidal heating is the cause of large radii, but that an eccentricity driving companion is not present, then either the system is in a transient period or that this thermal evolution model is not correct. On the other hand, if we rule out transient explanations, then either a constant heating is present or it is necessary to invoke another mechanism.

5.3. High Q'_s Cases

Although Q'_s is generally thought to be closer to 10^5 based on the observed circularization time in binaries, it is possible that tidal dissipation in the stars is less efficient in the planet–star case. Since tidal evolution is not fully understood, the high Q'_s case may or may not be physical. However, an advantage of this case is that it allows for orbital history solutions with a recent circularization. In this regime, the planet migrates inward at a slower rate and thus the circularization would occur at a later time. Also, after the tidal power is deposited, the planet is not rapidly migrating into the star as in the low Q'_s cases. Ibgui & Burrows (2009) have suggested that high Q'_s case can better explain the radius of HD 209458b.

We have explored this parameter regime as shown in Table 2 for five of the systems that we were not able to explain in the low Q'_s cases. We test the cases $Q'_s = 10^6$ and $Q'_s = 10^7$ with

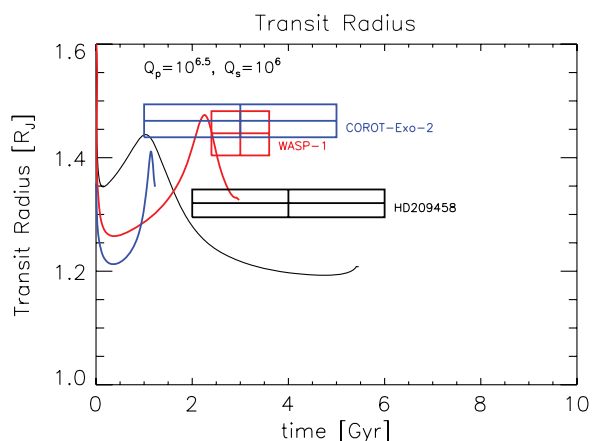


Figure 15. Potential radius evolution histories for HD 209458b, WASP-1b, and CoRoT-Exo-2b with no core, $Q'_p = 10^{6.5}$ and $Q'_s = 10^6$ (larger than our standard case). As usual, these evolution histories have been selected from an ensemble of possible initial conditions such that at some point during the estimated age of the system, the planet has orbital parameters that are consistent with the observed values.

(A color version of this figure is available in the online journal.)

both $Q'_p = 10^5$ and $Q'_p = 10^{6.5}$. In the table, the radius range is reported for a given core size, Q'_p and Q'_s model parameters, as well as the number of runs that were found at some point in time to be consistent with the observed age, semimajor axis, and eccentricity of the system.

Also, in Figure 14, we show snapshots in semimajor axis/eccentricity space of possible evolution histories of HD 209458b that are consistent with the observed parameters. The black points are the original orbital parameters, while the red points are the orbital parameters at a later time. The green oval is the 1σ orbital parameters. The dashed green line is the 3σ orbital parameters, which we require an evolution histories to fall within during the expected age range of the system. Eccentricity was sampled from 0.2 to 0.8 in this particular case.

We also show in Figure 15, possible radius evolution histories for the planets HD 209458b, WASP-1b, and CoRoT-Exo-2b. When Q'_s is allowed to be larger, the qualitative effect is that the planet's semimajor axis decreases slower and thus the circularization event occurs at a later time. This makes it possible to sometimes achieve higher radius values at the expected age of the system with the model. However, even for these high Q'_s runs for these large-radius planets, only for two of the five can the observed radius be matched.

6. DISCUSSION & CONCLUSIONS

This paper presents a coupled tidal and thermal evolution model applicable to close in extrasolar giant planets. The model is tested against 45 of the known transiting systems. Generally, tidal evolution yields two competing effects on the radii of close in extrasolar giant planets (EGPs).

1. Tidal evolution requires that, after planet formation and subsequent fast migration to a relatively close in orbit, the planet start at a larger semimajor axis than is currently observed (Jackson et al. 2008a). This results in less incident flux at earlier times, which allows the planet to cool more efficiently and contract more at a young age, which moves the range of feasible model radii at the current time to smaller values. Generally this is a minor effect, but it is

more important for cases when the current incident flux is larger.

2. Tidal evolution deposits energy into the planet when the orbit is being circularized. This typically increases the radius of the planet at this time. If there is an eccentricity driving source for the inner planet, then tidal heating can be important for the duration of the planet's life. If the planet starts with a highly eccentric orbit, it might not circularize for gigayears. The semimajor axis of the planet's orbit will initially slowly decrease due to tides on the star. As the planet moves closer to the star, tides on the planet become more effective. This delay of circularization can sometimes allow tidal heating to significantly inflate planets multiple gigayears after formation despite these systems having shorter "circularization" timescales.

We have shown that for the close in giant planets that orbital history can play a large role in determining the thermal evolution and current observed radius. While the effects are larger for planets with larger initial eccentricities, tidal evolution still affects the thermal evolution of planets with zero eccentricity as well. Varying amounts of time-dependent tidal heating are degenerate with the radius effects due to the core of a planet (or more generally, a heavy element enrichment).

Since at the current time we are ignorant of the exact orbital history, it is generally not possible to determine the mass of the core with complete confidence for any specific system. However, in cases when the radius of the planet is especially small, a large core or increased heavy element abundance is required. For larger radius planets, it is not possible to determine the planet's core size because recent tidal heating is degenerated with smaller core sizes. Furthermore, some systems likely have more complex orbital dynamics than described here due to the effects a third body. The uncertainty is increased since despite our expectation that tidal effects do occur, the rate that at which they occur (controlled by Q) is uncertain to an order of magnitude.

This paper serves as a *forward* test of the tidal theory for close in EGPs outlined by Jackson et al. (2008b), who had previously only investigated heating rates *backwards* in time, from current small eccentricities from 0.001 to 0.03. Quite often however, the forward modeling of these single-planet systems, across a wide swath of initial a and e , is not consistent with current eccentricities as large as Jackson et al. (2008b) assumed. If initial eccentricities were indeed large, then final circularization and tidal surge may indeed be fairly recent, but this cannot be expected to be the rule in these systems. We have taken an agnostic view as to whether initial migration to within 0.1 AU was via scattering or disk migration. In the former, initial eccentricities up to 0.8 are possible (Chatterjee et al. 2008) while in the latter the initial eccentricity would be zero. The viability of tidal heating to explain even some of the inflated planets with very small *current* eccentricities rests on the notion that planet scattering does occur, such that circularization (and radius inflation) can occur at gigayear ages. The detection of misalignment between the planetary orbital plane axis and stellar rotation axis via the Rossiter–McLaughlin Effect (e.g., Winn et al. 2007, 2008b) is beginning to shed light on migration. Fabrycky & Winn (2009) have found tentative evidence that is consistent with two modes of migration, one which may yield close alignment (perhaps from disk migration) and one with which may yield random alignment (perhaps from scattering), although to date only XO-3b in the published literature shows a large misalignment (Hébrard et al. 2008). Further measurements

will help to constrain the relative importance of these two modes of migration.

Most of the systems investigated do not require tidal heating to match their radius, but these systems can also be readily explained when including tidal evolution. Some of the planets investigated can be matched with tidal heating that could not be explained with a standard contraction model. Depending on the Q'_p value chosen, HAT-P-4, HAT-P-9, XO-4, HAT-P-6, OGLE-TR-211, WASP-4, WASP-12, TrES-3, HAT-P-7, and OGLE-TR-56 can all be explained with an evolution history with nonzero initial eccentricity. WASP-6 and WASP-12 can be explained by invoking a minimum eccentricity, which may suggest the presence of a companion. Other systems were not explained by the model for our chosen Q'_p values. This suggests that either Q'_p and Q'_s may be much different than our expectation or that other mechanisms are at work in these large-radius planets.

This work should be taken as a simplified analysis of how tidal evolution can affect a planet's thermal evolution. Strong quantitative conclusions should not be drawn because of the large uncertainties in the tidal evolution model, especially at large eccentricity. Also, the rate of tidal effects may be a very strong function of frequency. If this is the case, the planet may spend a lot of time at certain states where tidal effects are slow and rapidly pass through states where tidal effects are more rapid. If a constant Q value can even be applied, the actual value is highly uncertain. The Q values that we choose were meant only to span the range that we considered to be likely. The rate of tidal effects may depend on the interior structure of the planet and may be different for different exoplanets. Also, this analysis only takes into account orbit-circularization tidal heating.

The conclusion that should be drawn from this work is that a planet's tidal evolution history can play an important role on the planets' current radius, especially for systems that are born at semimajor axis less than 0.1 AU. In some cases, tidal heating could have inflated the radius of the planet in the recent past, even though tidal heating in the present might not be happening. In other cases, we were not able to explain the large-radius observations with our coupled tidal–thermal evolution model. This suggests that tidal heating will not be able to explain all of the large-radius planets, which has been a hope of some authors (Jackson et al. 2008b; Ibgui & Burrows 2009). For some of the planets that we are able to explain, we require a recent circularization, such that this model can only explain these observations if we are at a “special time” in its evolution. This has to be reconciled with the fraction of planets that have large radii that require such an explanation. Improved constraints on the eccentricities of these systems will better constrain recent tidal heating.

A more robust treatment of the effects of tidal heating on transiting planet radius evolution may require a coupling of the model presented here to a scattering/disk migration model, which could derive the statistical likelihood of various initial orbital a and e configurations, which would then serve as the initial conditions to subsequent orbital–tidal and thermal evolution. This is important because for any particular planetary system the orbital evolutionary history of the close in planet may be difficult to ascertain. Recently Nagasawa et al. (2008) have simulated the formation of hot Jupiters with a coupled scattering and tidal evolution code, and find a frequent occurrence of hot Jupiter planets. A further coupled undertaking of this sort, to be compared with an statistically significant number of transiting planets, could be performed in the future.

J.J.F. and N.M. are supported by NSF grant AST-0832769. We thank the referee, G. Chabrier, as well as E. Ford, D. Fabrycky, and S. Gaudi for their comments.

Note added in proof. The references for the radius values used for the planets are: HD 17156b (Winn et al. 2009), HD 147506b/HAT-P-2 (Bakos et al. 2007), HD 149026b (Winn et al. 2008a), HD 189733b (Bakos et al. 2006), HD 197286b/WASP-7 (Hellier et al. 2009), HD 209458b (Knutson et al. 2007), GJ 436b (Bean et al. 2008), TrES-1 (Winn et al. 2007c), TrES-2 (Holman et al. 2007), TrES-3 (Sozzetti et al. 2009), TrES-4 (Torres et al. 2008), XO-1 (Holman et al. 2006), XO-2 (Torres et al. 2008), XO-3 (Winn et al. 2008c), XO-4 (McCullough et al. 2008), XO-5 (Pál et al. 2009), HAT-P-1 (Winn et al. 2007a), HAT-P-3 (Torres et al. 2007), HAT-P-4 (Torres et al. 2008), HAT-P-5 (Torres et al. 2008), HAT-P-6 (Torres et al. 2008), HAT-P-7 (Pál et al. 2008), HAT-P-8 (Latham et al. 2008), HAT-P-9 (Shporer et al. 2009), HAT-P-10/WASP11 (Bakos et al. 2009), HAT-P-11 (Dittmann et al. 2009), WASP-1 (Charbonneau et al. 2007), WASP-2 (Charbonneau et al. 2007), WASP-3 (Gibson et al. 2008), WASP-4 (Gillon et al. 2009b), WASP-5 (Gillon et al. 2009b), WASP-6 (Gillon et al. 2009a), WASP-10 (Johnson et al. 2009), WASP-12 (Hebb et al. 2009), WASP-14 (Joshi et al. 2009), COROT-Exo-1 (Barge et al. 2008), COROT-Exo-2 (Alonso et al. 2008), COROT-Exo-4 (Moutou et al. 2008), OGLE-TR-10 (Pont et al. 2007), OGLE-TR-56 (Pont et al. 2007), OGLE-TR-111 (Winn et al. 2007b), OGLE-TR-113 (Torres et al. 2008), OGLE-TR-132 (Moutou et al. 2004), OGLE-TR-182 (Pont et al. 2008), and OGLE-TR-211 (Udalski et al. 2008).

REFERENCES

- Alonso, R., et al. 2008, *A&A*, 482, L21
 Bakos, G. Á., et al. 2006, *ApJ*, 650, 1160
 Bakos, G. Á., et al. 2007, *ApJ*, 670, 826
 Bakos, G. Á., et al. 2009, *ApJ*, 696, 1950
 Baraffe, I., Chabrier, G., Barman, T. S., Allard, F., & Hauschildt, P. H. 2003, *A&A*, 402, 701
 Baraffe, I., Selsis, F., Chabrier, G., Barman, T. S., Allard, F., Hauschildt, P. H., & Lammer, H. 2004, *A&A*, 419, L13
 Barge, P., et al. 2008, *A&A*, 482, L17
 Bean, J. L., Benedict, G. F., Charbonneau, D., Homeier, D., Taylor, D. C., McArthur, B., Seifahrt, A., Dreizler, S., & Reiners, A. 2008, *A&A*, 486, 1039
 Bodenheimer, P., Laughlin, G., & Lin, D. N. C. 2003, *ApJ*, 592, 555
 Bodenheimer, P., Lin, D. N. C., & Marling, R. A. 2001, *ApJ*, 548, 466
 Burrows, A., Hubeny, I., Budaj, J., & Hubbard, W. B. 2007, *ApJ*, 661, 502
 Burrows, A., Sudarsky, D., & Hubbard, W. B. 2003, *ApJ*, 594, 545
 Chabrier, G., & Baraffe, I. 2007, *ApJ*, 661, L81
 Charbonneau, D., et al. 2005, *ApJ*, 626, 523
 Charbonneau, D., Winn, J. N., Everett, M. E., Latham, D. W., Holman, M. J., Esquerdo, G. A., & O'Donovan, F. T. 2007, *ApJ*, 658, 1322
 Chatterjee, S., Ford, E. B., Matsumura, S., & Rasio, F. A. 2008, *ApJ*, 686, 580
 Deming, D., Seager, S., Richardson, L. J., & Harrington, J. 2005, *Nature*, 434, 740
 Dittmann, J. A., Close, L. M., Green, E. M., Scuderi, L. J., & Males, J. R. 2009, *ApJ*, 699, L48
 Faber, J. A., Rasio, F. A., & Willems, B. 2005, *Icarus*, 175, 248
 Fabrycky, D., & Tremaine, S. 2007, *ApJ*, 669, 1298
 Fabrycky, D. C., Johnson, E. T., & Goodman, J. 2007, *ApJ*, 665, 754
 Fabrycky, D. C., & Winn, J. N. 2009, *ApJ*, 696, 1230
 Ford, E. B., & Rasio, F. A. 2006, *ApJ*, 638, L45
 Ford, E. B., & Rasio, F. A. 2008, *ApJ*, 686, 621
 Fortney, J. J. 2008, in ASP Conf. Ser. 398, Extreme Solar Systems, ed. D. Fischer et al. (San Francisco, CA: ASP), 405
 Fortney, J. J., Lodders, K., Marley, M. S., & Freedman, R. S. 2008, *ApJ*, 678, 1419
 Fortney, J. J., Marley, M. S., & Barnes, J. W. 2007, *ApJ*, 659, 1661
 Fortney, J. J., Saumon, D., Marley, M. S., Lodders, K., & Freedman, R. S. 2006, *ApJ*, 642, 495

- Fortney, J. J., Sudarsky, D., Hubeny, I., Cooper, C. S., Hubbard, W. B., Burrows, A., & Lunine, J. I. 2003, *ApJ*, 589, 615
- Gibson, N. P., et al. 2008, *A&A*, 492, 603
- Gillon, M., et al. 2009a, *A&A*, 501, 785
- Gillon, M., et al. 2009b, *A&A*, 496, 259
- Gillon, M., et al. 2007, *A&A*, 472, L13
- Goldreich, P., & Soter, S. 1966, *Icarus*, 5, 375
- Gu, P.-G., Bodenheimer, P. H., & Lin, D. N. C. 2004, *ApJ*, 608, 1076
- Gu, P.-G., Lin, D. N. C., & Bodenheimer, P. H. 2003, *ApJ*, 588, 509
- Guillot, T., Burrows, A., Hubbard, W. B., Lunine, J. I., & Saumon, D. 1996, *ApJ*, 459, L35
- Guillot, T., & Showman, A. P. 2002, *A&A*, 385, 156
- Hansen, B. M. S., & Barman, T. 2007, *ApJ*, 671, 861
- Hebb, L., et al. 2009, *ApJ*, 693, 1920
- Hébrard, G., et al. 2008, *A&A*, 488, 763
- Hellier, C., et al. 2009, *ApJ*, 690, L89
- Holman, M. J., et al. 2006, *ApJ*, 652, 1715
- Holman, M. J., et al. 2007, *ApJ*, 664, 1185
- Hubbard, W. B., Fortney, J. J., Lunine, J. I., Burrows, A., Sudarsky, D., & Pinto, P. 2001, *ApJ*, 560, 413
- Ibguí, L., & Burrows, A. 2009, arXiv:0902.3998
- Jackson, B., Barnes, R., & Greenberg, R. 2009, *ApJ*, 698, 1357
- Jackson, B., Greenberg, R., & Barnes, R. 2008a, *ApJ*, 678, 1396
- Jackson, B., Greenberg, R., & Barnes, R. 2008b, *ApJ*, 681, 1631
- Johnson, J. A., Winn, J. N., Cabrera, N. E., & Carter, J. A. 2009, *ApJ*, 692, L100
- Joshi, Y. C., et al. 2009, *MNRAS*, 392, 1532
- Knutson, H. A., Charbonneau, D., Burrows, A., O'Donovan, F. T., & Mandushev, G. 2009, *ApJ*, 691, 866
- Knutson, H. A., Charbonneau, D., Noyes, R. W., Brown, T. M., & Gilliland, R. L. 2007, *ApJ*, 655, 564
- Latham, D. W., et al. 2008, arXiv:0812.1161
- Laughlin, G., Marcy, G. W., Vogt, S. S., Fischer, D. A., & Butler, R. P. 2005, *ApJ*, 629, L121
- Levrard, B., Correia, A. C. M., Chabrier, G., Baraffe, I., Selsis, F., & Laskar, J. 2007, *A&A*, 462, L5
- Levrard, B., Winisdoerffer, C., & Chabrier, G. 2009, *ApJ*, 692, L9
- Li, S., Miller, N., Lin, D., & Fortney, J. 2009, *Nature*, submitted
- Lin, D. N. C., Bodenheimer, P., & Richardson, D. C. 1996, *Nature*, 380, 606
- Liu, X., Burrows, A., & Ibguí, L. 2008, *ApJ*, 687, 1191
- Madhusudhan, N., & Winn, J. N. 2009, *ApJ*, 693, 784
- Mardling, R. A. 2007, *MNRAS*, 382, 1768
- McCullough, P. R., et al. 2008, *ApJ*, submitted (arXiv:0805.2921)
- Moutou, C., et al. 2008, *A&A*, 488, L47
- Moutou, C., Pont, F., Bouchy, F., & Mayor, M. 2004, *A&A*, 424, L31
- Nagasawa, M., Ida, S., & Bessho, T. 2008, *ApJ*, 678, 498
- Ogilvie, G. I., & Lin, D. N. C. 2004, *ApJ*, 610, 477
- Ogilvie, G. I., & Lin, D. N. C. 2007, *ApJ*, 661, 1180
- Pál, A., et al. 2008, *ApJ*, 680, 1450
- Pál, A., et al. 2009, *ApJ*, 700, 783
- Papaloizou, J. C. B., Nelson, R. P., Kley, W., Masset, F. S., & Artymowicz, P. 2007, in *Protostars and Planets V*, ed. B. Reipurth, D. Jewitt, & K. Keil (Tucson, AZ: Univ. Arizona), 655
- Peale, S. J. 2008, in *ASP Conf. Ser. 398, Extreme Solar Systems*, ed. D. Fischer et al. (San Francisco, CA: ASP), 281
- Pont, F., et al. 2007, *A&A*, 465, 1069
- Pont, F., et al. 2008, *A&A*, 487, 749
- Rasio, F. A., & Ford, E. B. 1996, *Science*, 274, 954
- Sato, B., et al. 2005, *ApJ*, 633, 465
- Saumon, D., Chabrier, G., & van Horn, H. M. 1995, *ApJS*, 99, 713
- Shporer, A., et al. 2009, *ApJ*, 690, 1393
- Sozzetti, A., et al. 2009, *ApJ*, 691, 1145
- Thompson, S. L. 1990, ANEOS—Analytic Equations of State for Shock Physics Codes, Sandia Natl. Lab. Doc. SAND89-2951 (Albuquerque, NM: Sandia National Lab./National Technical Information Service), <http://prod.sandia.gov/techlib/access-control.cgi/1989/892951.pdf>
- Torres, G., Winn, J. N., & Holman, M. J. 2008, *ApJ*, 677, 1324
- Torres, G., et al. 2007, *ApJ*, 666, L121
- Udalski, A., et al. 2008, *A&A*, 482, 299
- Ward, W. R. 1997a, *Icarus*, 126, 261
- Ward, W. R. 1997b, *ApJ*, 482, L211
- Weidenschilling, S. J., & Marzari, F. 1996, *Nature*, 384, 619
- Winn, J. N., & Holman, M. J. 2005, *ApJ*, 628, L159
- Winn, J. N., et al. 2007, *ApJ*, 665, L167
- Winn, J. N., et al. 2008b, *ApJ*, 682, 1283
- Winn, J. N., Henry, G. W., Torres, G., & Holman, M. J. 2008a, *ApJ*, 675, 1531
- Winn, J. N., et al. 2007a, *AJ*, 134, 1707
- Winn, J. N., Holman, M. J., & Fuentes, C. I. 2007b, *AJ*, 133, 11
- Winn, J. N., et al. 2009, *ApJ*, 693, 794
- Winn, J. N., Holman, M. J., & Roussanova, A. 2007c, *ApJ*, 657, 1098
- Winn, J. N., et al. 2008c, *ApJ*, 683, 1076
- Wisdom, J. 2008, *Icarus*, 193, 637
- Wu, Y., & Murray, N. 2003, *ApJ*, 589, 605